How volcanic eruption latitudes diversify surface climate responses

Seungmok Paik[1], Seung-Ki Min[2,3], Seok-Woo Son[4], Soon-Il An[1,2,5], Jong-Seong Kug[2,3], and Sang-Wook Yeh[6]

[1]Irreversible Climate Change Research Center, Yonsei University, Seoul, 03722, Korea
5   [2]Division of Environmental Science and Engineering, Pohang University of Science and Technology, Pohang, Gyeongbuk, 37673, Korea
[3]Institute for Convergence Research and Education in Advanced Technology, Yonsei University, Incheon, 21983, Korea
[4]School of Earth and Environmental Sciences, Seoul National University, Seoul, 08826, Korea
[5]Department of Atmospheric Sciences, Yonsei University, Seoul, 03722, Korea
10   [6]Marine Science and Convergence Engineering, Hanyang University, ERICA, Ansan, 15588, Korea

Correspondence to: Seung-Ki Min (skmin@postech.ac.kr) and Seok-Woo Son (seokwooson@snu.ac.kr)

Abstract. This study analyzes the influence of tropical, northern, and southern volcanic eruptions on the surface climate, focusing on the role of El Niño–Southern Oscillation and stratospheric polar vortex, using large-ensemble simulations of the
15   Community Earth System Model Last Millennium Ensemble. Typically, volcanic eruptions at different latitudes induce El Niño-like sea surface temperature anomalies over the equatorial eastern Pacific. However, the temporal variations and intensities differ. Such El Niño-like responses tend to amplify summer monsoon drying, which is stronger when followed by tropical eruptions than after northern and southern eruptions. Additionally, volcanic eruptions generate a stronger stratospheric polar vortex of varying magnitudes in both hemispheres. The strengthened Arctic polar vortex that occurs after tropical and
20   southern eruptions, accompanies a positive Arctic Oscillation response in boreal winter. This induces warmer and wetter surface conditions over northern Eurasia relative to the conditions before the eruptions. However, the Arctic polar vortex and associated surface responses are only weakly influenced by northern eruptions. This is consistent with the more poleward spread of volcanic aerosols and the reduced equatorward extension of planetary wave propagation in the lower stratosphere. These results suggest that volcanic eruptions modulate surface climate by warming the sea surface temperature over the
25   equatorial eastern Pacific and strengthening the stratospheric polar vortex but with diverse patterns depending on eruption latitudes.

1. Introduction

Volcanic eruptions in the tropics trigger the worldwide spread of sulfate aerosols oxidized from sulfur dioxide and scatter incoming solar radiation in the lower stratosphere, inducing overall cooling in the troposphere (Robock and Mao, 1995;
30   Robock, 2000). In the lower stratosphere, the sulfate aerosols absorb solar (near-infrared) and terrestrial radiation triggering the heating of the tropics as opposed to cooling (Lacis et al., 1992; Stenchikov et al., 1998). At the surface, tropical eruptions

decrease global land precipitation, particularly over summer monsoon regions in both hemispheres (Iles and Hegerl, 2014; Joseph and Zeng, 2011; Paik and Min, 2017, 2018; Trenberth and Dai, 2007).

It is well known that high-latitude eruptions lead to greater scattering of incoming solar radiation over the relevant hemisphere;
35   this is because stratospheric circulation retains most of the stratospheric volcanic aerosols in that particular hemisphere (Gao et al., 2008; Oman et al., 2005). Thus, a high-latitude eruption predominantly causes surface cooling in the hemisphere in which the eruption occurred, producing a large thermal gradient between the two hemispheres (Oman et al., 2005; Stevenson et al., 2016). Furthermore, the hemispheric thermal gradient causes the intertropical convergence zone (ITCZ) to shift to the warmer hemisphere (i.e., the hemisphere not experiencing the volcanic eruption). This in turn affects the El Niño–Southern
40   Oscillation (ENSO) and global surface air temperature and precipitation distributions (Liu et al., 2016; Stevenson et al., 2016; Zuo et al., 2018, 2019a).

Several recent studies have reported the significant impacts of tropical and high-latitude volcanic eruptions on ENSO (Adams et al., 2003; Lim et al., 2016; Liu et al., 2018; Maher et al., 2015; Paik et al., 2020; Pausata et al., 2015; Stevenson et al., 2016; Zuo et al., 2018). Typically, tropical eruptions drive an El Niño-like sea surface temperature (SST) pattern over the equatorial
45   eastern Pacific (Adams et al., 2003; Maher et al., 2015). The resultant circulation anomalies have been suggested to enhance South Asian drying and southwest United States wetting (Stevenson et al., 2016) as well as global summer monsoon drying (Paik et al., 2020). Several mechanisms have been suggested for the El Niño-like SST responses, including the role of an oceanic dynamic thermostat (Emile-Geay et al., 2008; Zuo et al., 2018), southward ITCZ shift (Lim et al., 2016), and Maritime Continent (MC) drying (Ohba et al., 2013; Paik et al., 2020; Wang et al., 2018). The El Niño-like responses have also been
50   consistently observed following northern eruptions, in which the majority of previous studies have related ENSO responses to the southward ITCZ shift (Liu et al., 2018; Stevenson et al., 2016; Zuo et al., 2018). Unlike northern eruptions, the reported ENSO response to southern eruptions is inconsistent across studies. For instance, proxy-based ENSO reconstructions indicate La Niña-like responses as opposed to El Niño-like responses (Liu et al., 2018), and climate models have yielded varying results. Liu et al. (2018) observed a central Pacific El Niño-like response to southern eruptions using Community Earth System Model
55   (CESM) simulations. Using the CESM-Last Millennium Ensemble (CESM-LME; Otto-Bliesner et al., 2016), Stevenson et al. (2016) observed La Niña and weak El Niño-like SST anomalies during the first and second winters (December to February; DJF) following southern eruptions, while Zuo et al. (2018) found a strong El Niño condition during the second DJF after removing volcanic cooling effects.

There is also evidence of the impact of volcanic eruptions on the polar stratosphere. The enhanced equator–to–pole temperature
60   gradient in the lower stratosphere in response to tropical eruptions enhances the polar vortex through thermal wind balance, which may induce positive Arctic Oscillation (AO)-like surface responses in the Northern Hemisphere (NH) extratropics (Robock and Mao, 1992). Previous studies have proposed that the volcanic aerosol-induced tropospheric thermal gradient, changes to stratospheric ozone (Stenchikov et al., 2002), and variations in planetary wave propagation (Azoulay et al., 2021; Bittner et al., 2016) also contribute to polar vortex strengthening. In terms of high-latitude eruptions, Oman et al. (2005)
65   reported minor responses of the polar vortex and unclear surface anomalies following the Katmai eruption, which occurred at

58° N. There is little clarity as to how southern eruptions affect the Arctic polar vortex and the AO in the troposphere. Although the influence of tropical and high-latitude volcanic eruptions on surface climate has been studied, the details of this influence remain obscured. This is particularly the case for southern eruptions. This study carries out a comprehensive evaluation of how the latitudes of volcanic eruptions affect surface air temperature and monsoon precipitation. In addition to equatorial SST

70   responses, Arctic polar vortex responses are analyzed using CESM-LME simulations, which allow multiple volcanic eruptions in the tropics and high latitudes.

The remainder of the paper is structured into three sections. Sect. 2 describes the model simulations and analysis methods used in this study. Sect. 3 presents the results, including the ENSO, polar vortex, and AO responses to volcanic eruptions at different latitudes. It also discusses the distinct influences of these climate variability responses on surface climate and the associated

75   physical mechanisms. Finally, Sect. 4 presents a summary and discussion of the results.

2. Data and analysis method

2.1 Climate model simulations

This study utilizes CESM-LME simulations (Otto-Bliesner et al., 2016), carried out with CESM1.1 at a relatively low resolution due to the intensive computational and time demands of the large ensemble (Stevenson et al., 2016). The model

80   resolution is approximately 2.5° × 1.9° in the atmosphere, while it varies from 1°–0.3° in the ocean. The CESM-LME is one of the largest ensemble simulations of the last millennium. It uses volcanic forcing derived from 54 Arctic or Antarctic ice core-based reconstructions that provide aerosol loadings as a function of month, latitude, and altitude for the previous 1500 years (Gao et al., 2008). All eruptions with unknown seasonality were assumed to be erupted in April (Gao et al. 2008).

A total of 17 ensemble simulations are used. Among them, 12 simulations are full forcing experiments (all-forcing), which

85   include solar insolation, orbital change, land-use/cover variation, volcanic eruptions, and greenhouse gases. In these simulations, the ozone concentration is fixed at the pre-industrial control value over the last millennium (850–1849). This indicates that CESM-LME does not consider the influence of stratospheric ozone depletion following eruptions, as demonstrated by Stenchikov et al. (2002). The remaining five simulations are based on volcanic-only forcing experiments. The influence of non-volcanic forcings (e.g., greenhouse gases) is found to be negligible when comparing results from the two

90   experiments (results not shown).

2.2 Epoch analysis

Following Stevenson et al. (2016), only the strongest 13 volcanic eruptions from 850 to 1849 are analyzed (Table 1) because these eruptions have a sufficient aerosol mass mixing ratio to minimize biases from variations in eruption size (i.e., Stevenson

95   et al., 2016; Zuo et al., 2018, 2019a, b). The selected eruptions are divided into tropical, northern, and southern eruptions based on the latitude of each volcanic eruption (Gao et al., 2008); four tropical, six northern, and three southern eruptions are

identified (Table 1). Northern eruptions have an aerosol mixing ratio that is 1.7 times larger in the NH than in the Southern Hemisphere (SH), one year after an eruption. The opposite is true for southern eruptions, while tropical eruptions have a NH to SH aerosol loading ratio of 0.77–1.20.

100

Table 1: List of year 0 for tropical, northern, and southern eruptions. Year 0 corresponds to the eruption year, while 1762 (Laki) eruption occurred at September 1761.

Class	Year 0
Tropical eruption	1258 (Samalas), 1284, 1809, 1815 (Tambora)
Northern eruption	1176, 1213, 1600, 1641, 1762 (Laki*), 1835
Southern eruption	1275, 1341, 1452 (Kuwae)

*The Laki eruption was assigned an incorrect date in Gao et al. (2008); the true date is 1783 (Stevenson et al., 2016).

105 Climate responses are quantified using relative change from 5 y pre-eruption averages. An exception to this is the 1815 Tambora eruption, in which the 5 y pre-eruption average prior to the 1809 eruption is used to exclude the influence of the 1809 eruption. Once the anomalies are quantified, the climate responses to volcanic eruptions are averaged separately for the tropical, northern, and southern eruptions. Each ensemble simulation is considered independent. As such, climate responses to tropical eruptions are computed from 68 simulations (4 eruptions × 17 ensembles). The year 0 is defined (YR0) as the calendar year 110 when the volcanic aerosol mass reaches its peak (Table 1). To analyze seasonal responses, May to October (MJJASO) is defined as the boreal summer (austral winter), and November to April (NDJFMA) as boreal winter (austral summer). The statistical significance of climate responses is tested using a Monte Carlo method. Once the centered 5 y pre-eruption anomalies for each eruption are aggregated (i.e., 510 samples for northern eruptions from 5 y × 6 eruptions × 17 ensembles), this is repeated 10,000 times using the average for randomly selected anomalies (e.g., 102 samples for northern eruptions from 6 115 eruptions × 17 ensembles). The 95 % confidence interval (CI) is then estimated as the 2.5th to 97.5th percentiles of randomly driven responses. Responses are considered statistically significant when anomalies are beyond the 95 % CI.

3. Results

3.1 Volcanic radiative forcing and surface temperature responses

Radiative forcing is first compared between volcanic eruptions at different latitudes. Figures 1(a), (d), and (g) illustrate the 120 composite patterns of zonal-averaged top-of-atmosphere (TOA) net shortwave radiation anomalies from tropical, northern, and southern eruptions, respectively. Tropical eruptions exhibit symmetric decreases in shortwave radiation from the equator. In contrast, northern and southern eruptions exhibit maximum shortwave radiation decreases in the hemisphere of the eruption. The shortwave radiation decreases from southern eruptions also extend into the NH tropics. Importantly, high-latitude responses are delayed for several months to years in both hemispheres, as a result of proliferating volcanic aerosols from

125   stratospheric transport (Gao et al., 2008). In terms of intensity, northern eruptions exhibit relatively weaker radiative forcing than other eruptions.
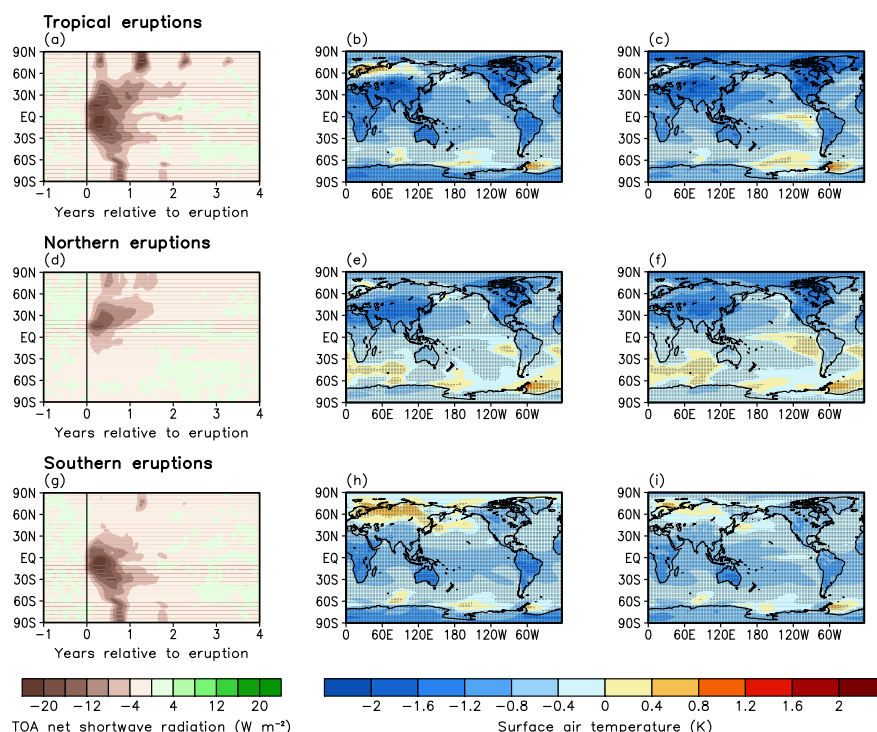
Figure 1: (a, d, g) Temporal composites of zonally averaged top of atmosphere net shortwave radiation anomalies for (a) tropical; (d) northern; and (g) southern volcanic eruptions. Vertical black line represents April of Year 0; (b, c, e, f, h, i) post-eruption subsequent (b, e, h) first; and (c, f, i) second 12 month-averaged surface air temperature anomalies for (b, c) tropical; (e, f) northern; and (h, i) southern eruptions. Black dots indicate regions which show a significant response beyond the 95 % confidence interval.

Consistent volcanic forcings are obtained from the column-integrated volcanic aerosol mass reported by Gao et al. (2008) (Fig. S1). An increasing volcanic aerosol mass due to northern eruptions is observed prior to April of YR0 (Fig. S1(b)). This aerosol

135   mass largely disappears when the 1762 Laki eruption is discarded (Figs. S1(d) and S2). The influence of seasonality on individual eruptions is discussed in details in Sect. 3.3.1. Although the amount of volcanic aerosol mass on average differs between tropical, northern, and southern eruptions (Figs. S1(a)–(c)), some individual eruptions generate very similar quantities of aerosol injection mass (Figs. S3(a), (c), (e)). Tropical, northern, and southern eruptions are characterized by distinct

meridional volcanic aerosol distributions in the upper troposphere and lower stratosphere, with the former having more

140 aerosols in subtropical to high-latitude regions (Figs. S3(b), (d), (f)).

Consistent with the latitudinal structure of incoming solar radiation reduction, marked surface air temperature decreases are observed over the global land mass in the subsequent first and second years following tropical eruptions (Figs. 1(b), (c)). In contrast, northern and southern eruptions have a stronger cooling effect over the relevant hemisphere in the two years after the eruptions, with different responses over the equatorial Pacific and northern Eurasia (Figs. 1(e), (f), (h), (i)).

145

3.2 ENSO and global monsoon precipitation responses

3.2.1 ENSO response

Figure 2(a) shows the equatorial SST responses (shadings; averaged over 5° S–5° N) from tropical eruptions, which also presents the relative SST (RSST; contours), which has been defined as local SST minus the tropical average SST (20° S to 20°

150 N). The RSST effectively represents ENSO variation in the context of a volcanic cooling influence (Khodri et al., 2017; Zuo et al., 2018). The results show that tropical eruptions have a relatively stronger cooling effect over the eastern Pacific than the central Pacific for approximately two seasons following volcanic eruptions. This La Niña-like SST (or RSST) pattern may occur because of the shallower mixed layer depth over the equatorial eastern Pacific than its western to central counterparts (McGregor and Timmermann, 2011; Paik et al., 2020). The analysis of the simple ocean mixed-layer temperature budget

155 supports this argument, in which smaller differences in mixed-layer temperature anomalies between the eastern and central Pacific occur only when a spatially uniform mixed-layer depth is assumed (Fig. S4). After the first boreal winter following volcanic eruptions, strong El Niño develops over the equatorial eastern Pacific.
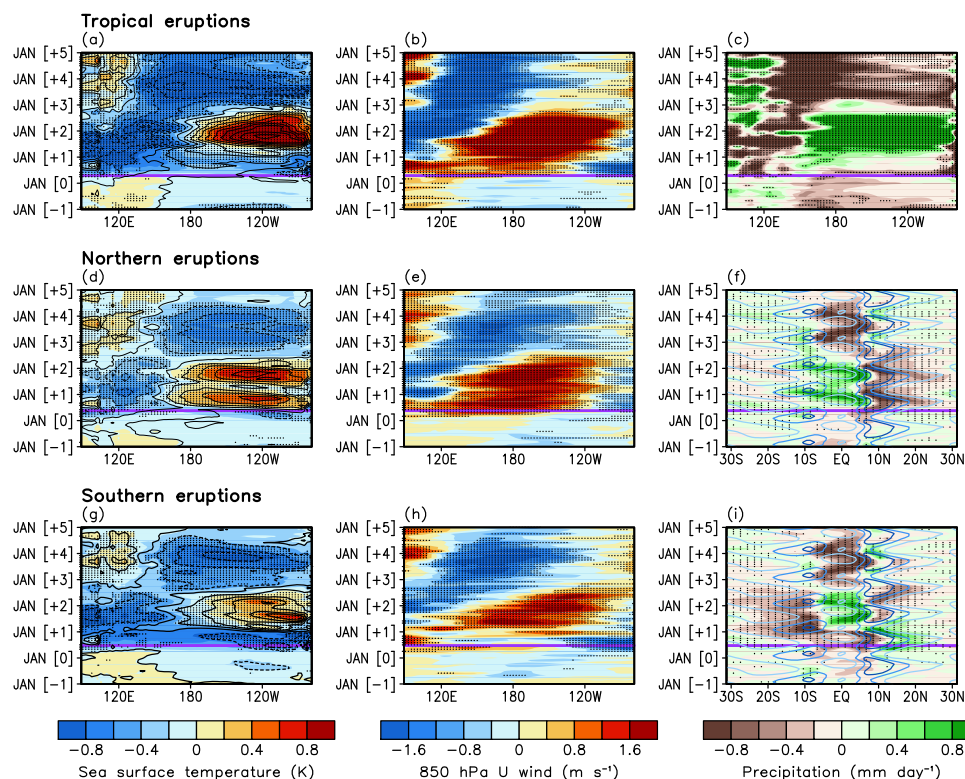
Figure 2: Meridional (5° S to 5° N) ((f, i) zonal (120° E–90° W)) averaged (a, d, g) SST (shading); RSST (contours, interval: 0.2 K); (b, e, h) 850 hPa zonal wind; and (c, f, i) precipitation anomalies associated with (a–c) tropical; (d–f) northern; and (g–i) southern volcanic eruptions. Thick purple horizontal lines indicate that April of Year 0, which includes most of the volcanic eruptions activated in CESM-LME. Black dots indicate areas which exhibit significant responses beyond the 95 % confidence interval, representing consistency for RSST in (a), (d), and (g). Blue contours in (c), (f), and (i) represent climatology of precipitation for 3, 6, and 9 mm d^{-1} (greater values with darker blue).

The mixed-layer temperature budget analysis results (Fig. S4) indicate that volcanic-induced El Niño cannot simply be attributed to radiation, Newtonian damping, and dynamic thermostat mechanisms. The El Niño responses are instead due to variations in ocean dynamical processes and air–sea feedbacks. As such, the physical mechanisms of El Niño development following eruptions are further evaluated. The 850-hPa zonal wind responses are well matched with SST or RSST responses (Fig. 2(b)), revealing easterly wind anomalies from the equatorial eastern Pacific after eruptions associated with La Niña-like SST cooling and westerly anomalies over the equatorial western Pacific. The westerly winds increase in strength during the boreal winter and propagate into the equatorial eastern Pacific (Fig. 2(b)), eventually inducing El Niño-like SST warming (Fig.

Atmospheric
Chemistry
and Physics
Discussions
Open Access
EGU

2(a)) through the Bjerknes feedback. The westerly anomalies are largely related to MC drying (Fig. 2(c)), which is generated

175 from stronger cooling over the MC than the surrounding ocean as a result of its lower heat capacity (Eddebbar et al., 2019; Ohba et al., 2013; Paik et al., 2020; Wang et al., 2018). Although tropical precipitation and surface temperature anomalies exhibit La Niña-like patterns in the subsequent six months following eruptions, MC drying remains evident (Figs. S5(a), (b)). Moreover, significant inter-simulation correlations are observed between MC drying and El Niño responses (Figs. S5(c), (d)), indicating the important role of MC drying in El Niño development following tropical eruptions.

180 Figures 2(d)–(f) illustrate the results for northern eruptions. After these eruptions, El Niño-like warming and strong westerly winds appear during the YR0 boreal summer (Figs. 2(d), (e)). The responses persist for a year after eruptions with double peaks, consistent with Zuo et al. (2018). The zonal-mean precipitation responses (Fig. 2(f)) indicate a southward shift in the ITCZ following northern eruptions, resulting in increased precipitation over the southern parts of the ITCZ. The seasonal cycle of the southward ITCZ shift may have caused seasonal variations in the El Niño-like equatorial eastern Pacific warming (Fig.

185 2(d)).

The equatorial Pacific climate responses to southern eruptions are shown in Figs. 2(g)–(i). Strong La Niña-like SST (and RSST) cooling occurs in the equatorial eastern Pacific after southern eruptions, followed by El Niño-like warming at YR+1 (Fig. 2(g)), with strong westerly winds (Fig. 2(h)). Similar to tropical eruptions, the initial La Niña-like SST (and RSST) cooling is largely due to the shallower mixed-layer depth in the equatorial eastern Pacific, whereas subsequent El Niño-like SST warming cannot

190 simply be attributed to the dynamic thermostat mechanism (results not shown). The increased reduction in solar radiation and surface temperature cooling over the SH following southern eruptions (Figs. 1(g)–(i)) trigger a strong northward shift in the ITCZ (Fig. 2(i)). The precipitation responses over the equatorial regions are more complex, showing large seasonal fluctuations for several months after eruptions. Thus, a more detailed analysis of the YR0 response is required to understand how El Niño occurs at YR+1 following southern eruptions.

195 Figures 3(a), (b) illustrate the precipitation and 850 hPa horizontal wind responses for two seasons following southern eruptions (i.e., April to June (AMJ) and July to September (JAS) of YR0). During AMJ, easterly winds prevail along the equatorial eastern Pacific in association with the La Niña-like SST anomalies and the anomalous drying and divergence from northern South America. In the equatorial western to central Pacific, westerly winds prevail potentially because of MC drying (Fig. 3(a)). Note that drying is relatively weak at the equatorial central Pacific because of the northward shift of the South Pacific

200 Convergence Zone (SPCZ) in AMJ. Additionally, the greater eastward expansion of the SPCZ enhances wetting over the equator, contributing to stronger westerly winds during that season (Fig. 3(a)). During JAS, only easterly winds are dominant over the equatorial eastern Pacific (Fig. 3(b)). This seems to be partly related to the seasonal cycle of the ITCZ that has a relatively northward location in JAS than AMJ, which may potentially shift MC drying and ITCZ further northward.
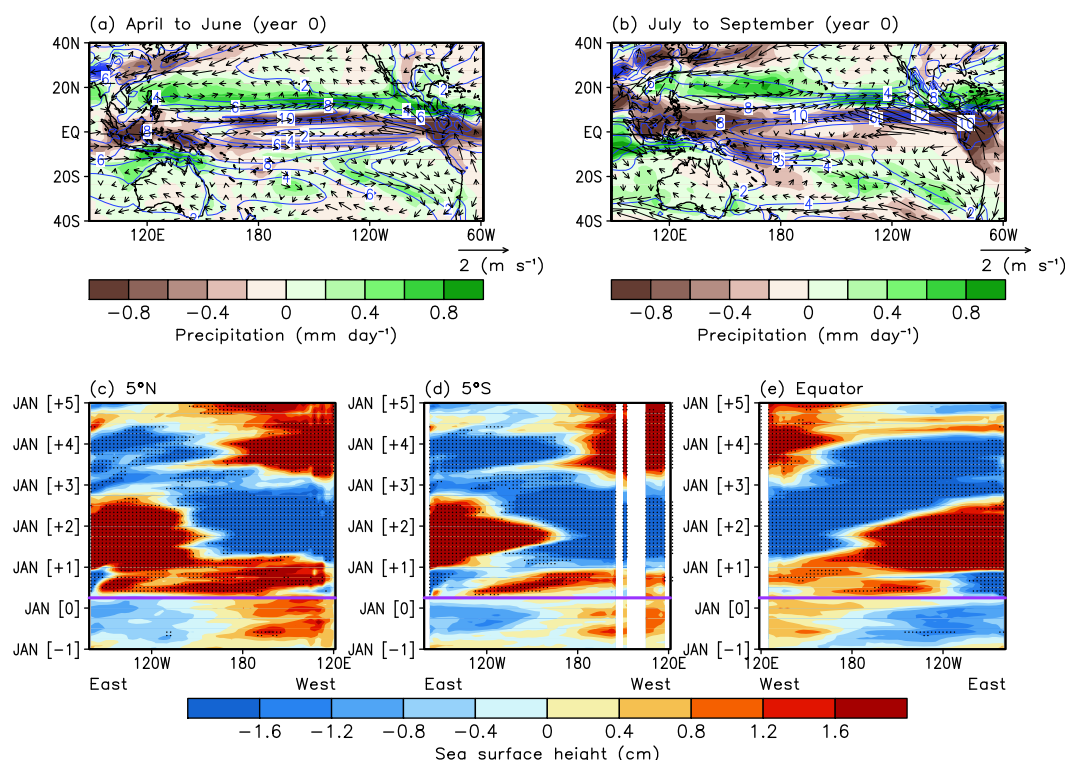
Figure 3: (a, b) Year 0 (a) April to June (AMJ) and (b) July to September (JAS) precipitation (shading) and 850 hPa horizontal wind (vector, unit: m s⁻¹) anomalies associated with southern eruptions; (c–e) sea surface height anomalies associated with southern volcanoes over the Pacific at (c) 5° N; (d) 5° S; and (e) the equator. Horizontal purple lines indicate the April of Year 0. Black dots indicate areas in which significant responses occur beyond the 95 % confidence interval.

After southern eruptions, the La Niña-like SST-induced easterly winds prompt the westward downwelling Rossby wave propagation of sea surface height at 5° N and 5° S (Figs. 3(c), (d)). In contrast, eastward downwelling Kelvin waves appear at the equator as a result of the westerly winds that occur immediately after eruptions (Fig. 3(e)). However, these waves are largely negated by the strong easterly winds in the equatorial eastern Pacific (Fig. 2(h)). Following these events, reflected downwelling Kelvin waves develop over the equatorial western Pacific (Battisti and Hirst, 1989), which propagate to the equatorial eastern Pacific, causing El Niño during YR+1 after southern eruptions. The sea surface height variations are also well supported by the 20 °C isotherm depth anomalies (Fig. S6). These results support the oscillation mechanism from the initial La Niña-like SST (McGregor and Timmermann, 2011) to El Niño development at YR+1 for southern eruptions.

In short, distinct ENSO-like SST fluctuations occur after tropical, northern, and southern eruptions, in which the eruptions typically trigger significant El Niño responses at YR+1 or YR0 (for northern eruptions only). El Niño responses are found to

220   be due to MC drying, a southward ITCZ shift, or delayed oscillation mechanisms (Figs. 2 and 3), with limited influences of ocean dynamical processes or air-sea feedback (Fig. S4).

3.2.2 Global monsoon precipitation response and ENSO influence

This subsection further investigates how a variety of El Niño responses under different eruption latitudes affect global monsoon

225   precipitation. Although Paik et al. (2020) reported that the El Niño induced by strong tropical eruptions influences global monsoon drying responses, their difference among volcanic eruptions at different latitudes has not been thoroughly examined. To analyze the effect on precipitation over the global monsoon region, the global land monsoon domain (Fig. 4(a)) is defined as the area in which the annual variation in precipitation (difference between local summer and winter precipitation) is >2 mm d^{-1}, and local summer precipitation exceeds 55% of the annual precipitation (Hsu et al., 2011; 2013) averaged for the 1100–

230   1849 period. This shows that CESM-LME represents the global monsoon domain containing the monsoons that occur in Africa, Asia, Australia, and the Americas. Figure 4(b) shows the responses in the NH and SH summer monsoon precipitation to tropical eruptions. A large decrease in summer monsoon precipitation is found in both hemispheres at similar magnitudes. In contrast, precipitation primarily decreases in the NH summer monsoon regions following northern eruptions because solar radiation reduction and surface cooling are stronger in the NH (Fig. 4(c)). The magnitude of drying in the NH following

235   northern eruptions is comparable to that after tropical eruptions, although solar radiation perturbations are weaker after the former than the latter (Figs. 1(a), (d)). This is likely due to a larger ITCZ displacement after northern eruptions (Fig. 2(f)). After southern eruptions, precipitation largely decreases in the SH monsoon regions with a slightly stronger amplitude than tropical eruptions (Fig. 4(e)). Unlike northern eruptions, southern eruptions also induce weak drying in the NH, reflecting the reduced asymmetric forcing pattern (Figs. 1(d), (g)).
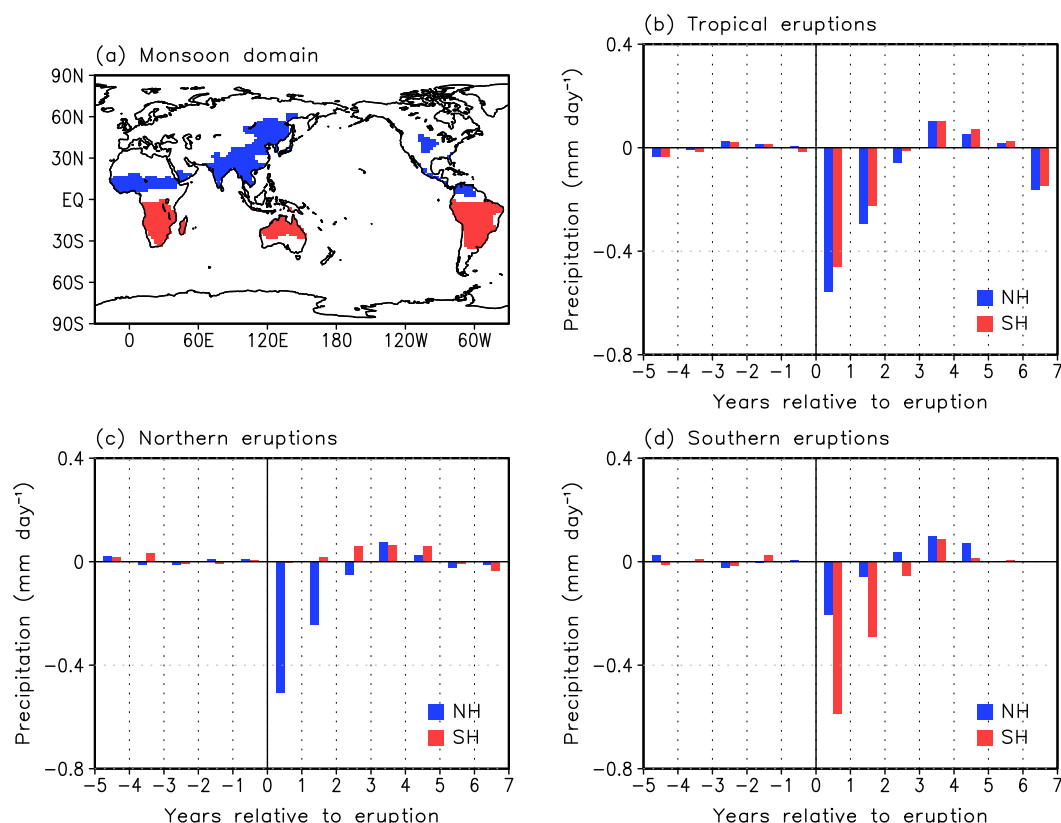
240

Figure 4: (a) Spatial pattern of global monsoon area defined using 17 ensemble mean of CESM-LME. NH and SH summer monsoon regions are depicted using blue and red colors, respectively; (b–d) timeseries of NH (blue) and SH (red) summer monsoon regional precipitation associated with (b) tropical; (c) northern; and (d) southern volcanoes from 17 ensemble mean of CESM-LME.

245

Figures 5(a), (b) illustrate the regression coefficients between precipitation and the Niño-3.4 RSST for the boreal and austral summer during the 1100–1849 period, respectively. It shows that CESM-LME is able to reliably capture ENSO-related precipitation anomalies as shown by Dai and Wigley (2000) (e.g., drying for the monsoons in India, Australia and the Americas). Figure 5(c) compares the probability density functions (PDFs) of monsoon precipitation responses from tropical

250 eruptions using raw data with those in which the El Niño influence is removed. Here the El Niño influences are estimated using linear regression. After removing the ENSO influence, the NH and SH summer monsoon drying is significantly reduced by 52.5 % and 62.1%, respectively ($P < 0.01$ based on t test), alongside the ensemble spread of precipitation responses (i.e.,

11

PDF spread) (P <0.01 based on F test). These results are consistent with the findings from Paik et al. (2020), supporting the important role of volcanic aerosol-induced El Niño and its influence on global monsoon precipitation.

255 Following northern eruptions, the El Niño contribution to the reduction in NH monsoon precipitation becomes weaker, explaining only ~9 % and 33 % of the precipitation decrease at YR0 and YR+1, respectively. The drying responses are only significantly reduced at YR+1 when removing the ENSO influence (P <0.01, based on the t-test) (Fig. 5(d)). Furthermore, the ensemble spread is significantly reduced after removing the ENSO influence (P <0.01 for YR0; P = 0.04 for YR+1, based on the F-test). This relatively weaker ENSO influence is due to the weaker El Niño intensity after northern eruptions compared

260 to tropical eruptions (Figs. 2(a), (d)), although there was a comparable precipitation decrease (Figs. 4(b), (c)) because of the large southward ITCZ displacement. The El Niño that occurs at YR+1 in response to southern eruptions contributes to the decrease in SH monsoon drying, although this is weaker (approximately 24.0 % based on mean response, Fig. 5(e)) when compared to tropical and northern eruptions. The weaker influence of El Niño on the SH monsoon precipitation response is likely caused by the reduced El Niño intensity, while strong drying occurs over the SH monsoon regions (Fig. 4(d)).
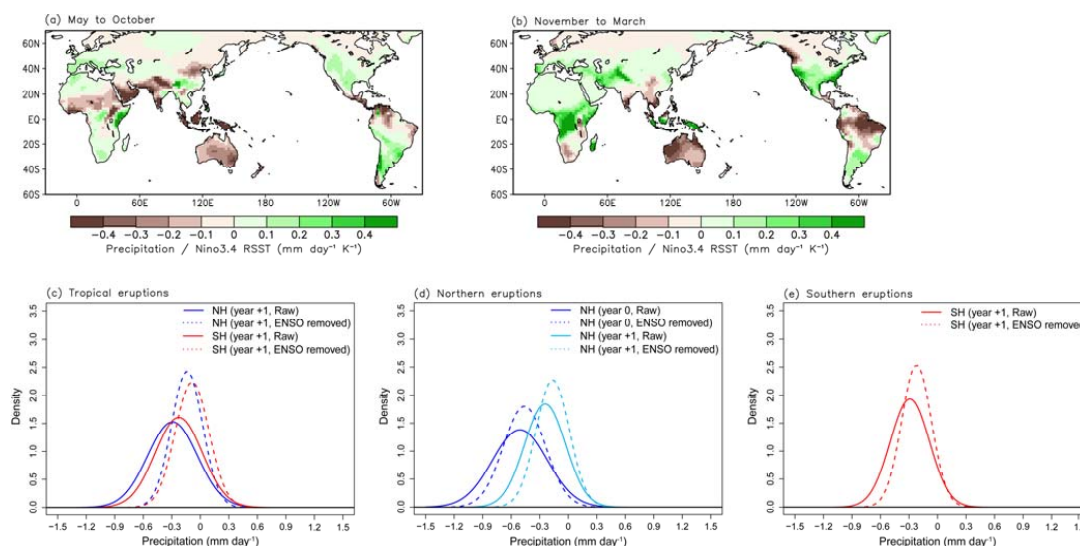
265

Figure 5: (a–b) 17 ensemble-averaged spatial pattern of regression coefficients between the gridded precipitation and Niño3.4 RSST for (a) boreal summer; and (b) austral summer for the 1100–1849 period; (c–e) normalized probability density function of CESM-LME 17 ensembles for the precipitation responses of individual eruptions over (c) NH and SH monsoon for tropical eruptions; (d)
270 NH monsoon for northern eruptions; and (e) SH monsoon for southern eruptions during peak El Niño occurrence periods from raw data (solid lines) and that with the El Niño influence removed (dashed lines). Year +1 refers to tropical and southern eruptions, whereas years 0 and +1 refers to northern eruptions.

3.3 Polar vortex, AO, and surface climate responses

275 **3.3.1 Polar vortex response**

Volcanic eruptions significantly modulate the stratospheric polar vortex. Following tropical eruptions, tropical temperatures in the lower stratosphere rapidly increase (Fig. 6(a)) through the absorption of near-infrared and terrestrial radiation. This causes a strong meridional temperature gradient centered at 25–30° N in the NH. In the SH, the maximal temperature gradient initially occurs at the subtropics and then propagates poleward. The associated zonal-mean wind anomalies at 10 hPa show the

280 enhancement of westerly winds in the subtropics, where the maximum temperature gradient exists after eruptions (Fig. 6(b)). During the boreal winter, a separate wind maximum appears at approximately 70° N, as shown by Bittner et al. (2016). This strengthening of the polar vortex cannot simply be attributed to the volcanic aerosol-induced temperature change.
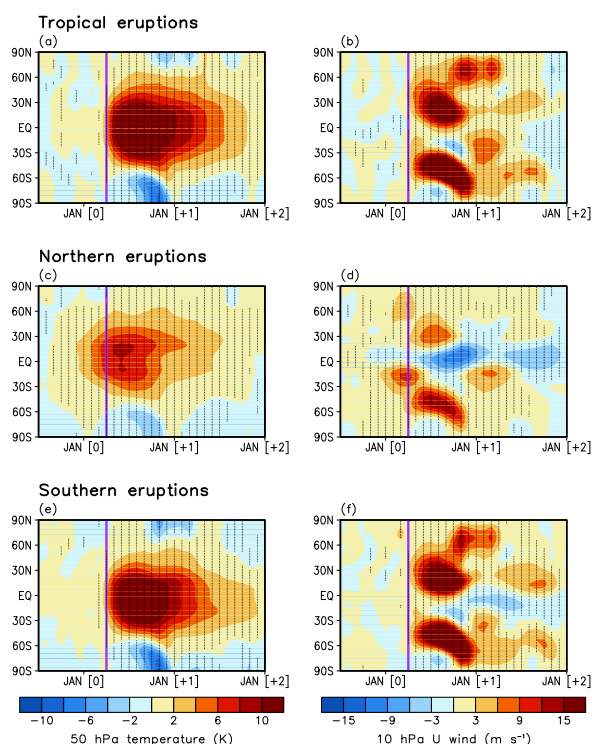

285 **Figure 6: Zonally averaged (a, c, e) 50 hPa temperature; and (b, d, f) 10 hPa zonal wind anomalies following (a, b) tropical; (c, d) northern; and (e, f) southern eruptions. Thick purple horizontal lines indicate April of Year 0. Stippling indicates areas in which the anomalies extend beyond the 95 % confidence interval.**

Figure 6(c) shows that northern eruptions also cause warming of the lower stratosphere, although the overall responses are

290   weaker. It occurs slightly northward compared to that of tropical eruptions, consistent with the aerosol distribution (Fig. S1(b)). As a result, the maximum temperature gradient is more poleward in the NH and equatorward in the SH than following tropical eruptions. The corresponding zonal wind anomalies are found at similar latitudes (Fig. 6(d)). Unlike tropical eruptions, Arctic polar vortex enhancement is not evident during the boreal winter following northern eruptions (Fig. 6(d)). It is unlikely that the insignificant Arctic polar vortex change is a result of volcanic forcing (Fig. 1(d)). The southern eruptions trigger a greater

295   change in lower stratospheric temperature in the SH than in the NH (Fig. 6(e)). However, the Arctic polar vortex responses are much stronger than those following northern eruptions, and almost comparable to those after tropical eruptions (Figs. 6(f)). Examination of individual northern eruptions shows that the Arctic polar vortex responses are insignificant in most cases (Fig. S7). An exception is the 1762 Laki eruption (Fig. S7(e)), which had strong enhancement of the Arctic polar vortex during the boreal winter of YR-1. This distinct response is mainly due to the timing of the eruption. The Laki eruption occurred in

300   September of YR-1, and there was insufficient time for volcanic aerosols to propagate to the polar regions. Also, stratospheric transport from extra-tropics to polar regions is weaker in winter (Gao et al., 2008) (Fig. S2(e)). Therefore, the aerosols increase the lower stratospheric temperature in the subtropics and mid-latitudes, generating a large meridional temperature gradient ~60–70° N (not shown), and enhancing the Arctic polar vortex in the boreal winter of YR-1 after the Laki eruption.

The southern eruptions show comparable polar vortex responses to tropical eruptions, as discussed above (Figs. 6(b), (f)).

305   Although changes in the lower stratospheric temperature in the NH differ slightly between southern and tropical eruptions (comparing Figs. 6(a) and (e)), the Arctic polar vortex is significantly strengthened in both cases (Figs. 6(b), (f)). These results are also consistent with those for individual tropical and southern eruptions (Figs. S8). However, some cases have a volcanic aerosol mass injection comparable to that of northern eruptions (Figs. S3(a), (c), (e)). This result indicates that the polar vortex response is not strongly dependent on volcanic forcing intensity.

310   Notably, the tropical, northern, and southern eruptions induce qualitatively similar stratospheric wind changes in the SH (Figs. 6(b), (d), (f)). This means that different polar vortex responses to volcanic eruptions at various latitudes are only unique in the NH. Therefore, it is important to consider what determines such unique polar vortex responses in the NH. Figure 7 illustrates the vertical profile of zonal wind in D_0JF_{+1} [December of YR0 to February of YR+1] and Eliassen-Palm (EP) flux anomalies in ON_0 [October and November of YR0] and in D_0JF_{+1} following volcanic eruptions. Figure 7(a) shows an enhanced lower

315   stratospheric polar vortex in the NH polar region after tropical eruptions. Strong westerly winds also appear in the subtropical lower stratosphere, as shown in Fig. 6(b). Tropospheric easterly anomalies, extending from the equatorial upper troposphere to the subtropical mid-troposphere, also occur in response to tropical tropospheric cooling and subtropical upper (middle) tropospheric warming (weaker cooling) (Fig. S9(a)). The subtropical upper tropospheric warming occurs due to the presence of volcanic aerosols in the subtropical upper troposphere (Fig. S3(b)). The EP flux anomalies show equatorward wave

320   propagation during ON_0 and D_0JF_{+1} (Figs. 7(b), (c)), potentially because of the enhanced westerly winds in the subtropical lower stratosphere (Fig. 6(b)). Holton and Tan (1980) demonstrated that westerly winds in the tropics allow Rossby waves to

propagate deep into the tropics by shifting the critical latitude equatorward. This Holton–Tan effect results in EP flux convergence at mid-latitudes and divergence at high latitudes. The EP flux divergence pattern shown in Figs. 7(b), (c) is indeed consistent with the Holton–Tan effect, and may be attributable to Arctic polar vortex strengthening. The same results are found

325 after southern eruptions (Figs. 7(g)–(i)). Unlike tropical and southern eruptions, northern eruptions exhibit easterly wind anomalies in the tropical lower stratosphere (Fig. 7(d)). This does not facilitate significant changes in the EP flux, and the EP flux divergence is too weak to alter the polar vortex (Figs. 7(e), (f)). This result suggests that zonal wind change in the subtropical stratosphere is likely a key factor that determines Arctic polar vortex changes in response to volcanic eruptions.
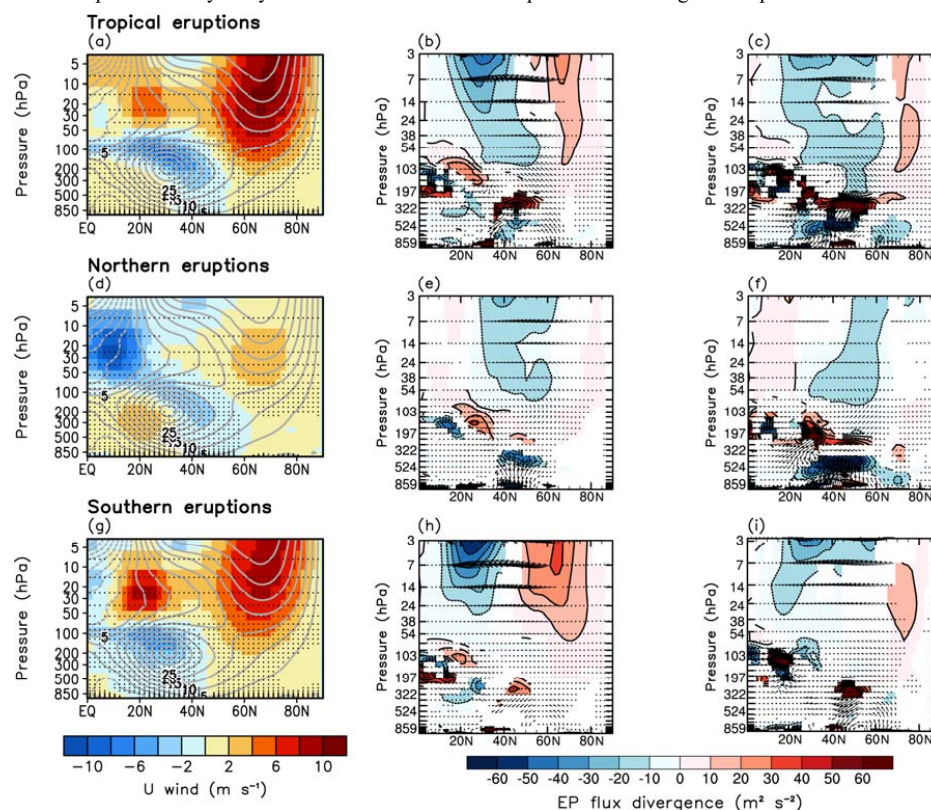

330 Figure 7: Zonally averaged vertical profile of (a, d, g) zonal wind during December of Year 0 to February of Year +1 (D_0JF_{+1}); and EP flux anomalies direction (vector) and its divergence (shading) during (b, e, h) October and November of Year 0 and (c, f, i) D_0JF_{+1} for (a–c) tropical; (d–f) northern; and (g–i) southern eruptions. Stippling indicates areas where the significant responses occur beyond the 95 % confidence interval; (a, d, g) gray contours indicate vertical profile of climatological (averaged for 1100–1849 period) boreal winter zonal wind.

335

3.3.2 Polar vortex and tropospheric circulation

Figure 8(a) presents the PDFs of normalized daily 10-hPa zonal wind anomalies, averaged from 60° N to 70° N during the DJF of the pre-eruption five years (black) and during D_0JF_{+1} after tropical eruptions (red). The probability of strong polar vortex events (or polar vortex strengthening events) beyond +2 standard deviations becomes much larger after tropical eruptions (17.84 %) than pre-eruption winters (1.07 %). More frequent strong polar vortex events can affect lower tropospheric circulation, as discussed by Baldwin and Dunkerton (2001) and Thompson et al. (2002). Figure 8(b) presents a composite analysis of strong polar vortex events. Here, we aggregate a total of 48 samples that have 10-hPa zonal wind anomalies greater than +2 standard deviations during the subsequent 5 d (its initial date was defined as '0 d') at D_0JF_{+1} with at least 60 d intervals between samples. Figure 8(b) shows the vertical profile of zonal wind anomalies from four vertical layers (850, 500, 200, and 10 hPa) before and after the composited 48 strong polar vortex events. By definition, the lower stratosphere westerlies are strongest during the first few days from the initial date (from 0 to 4 d). A few days later, they are followed by maximum lower tropospheric wind anomalies. This result supports the delayed influence of Arctic polar vortex enhancement on lower tropospheric circulation. A similar result is also observed after southern eruptions (Figs. 8(c), (d)).
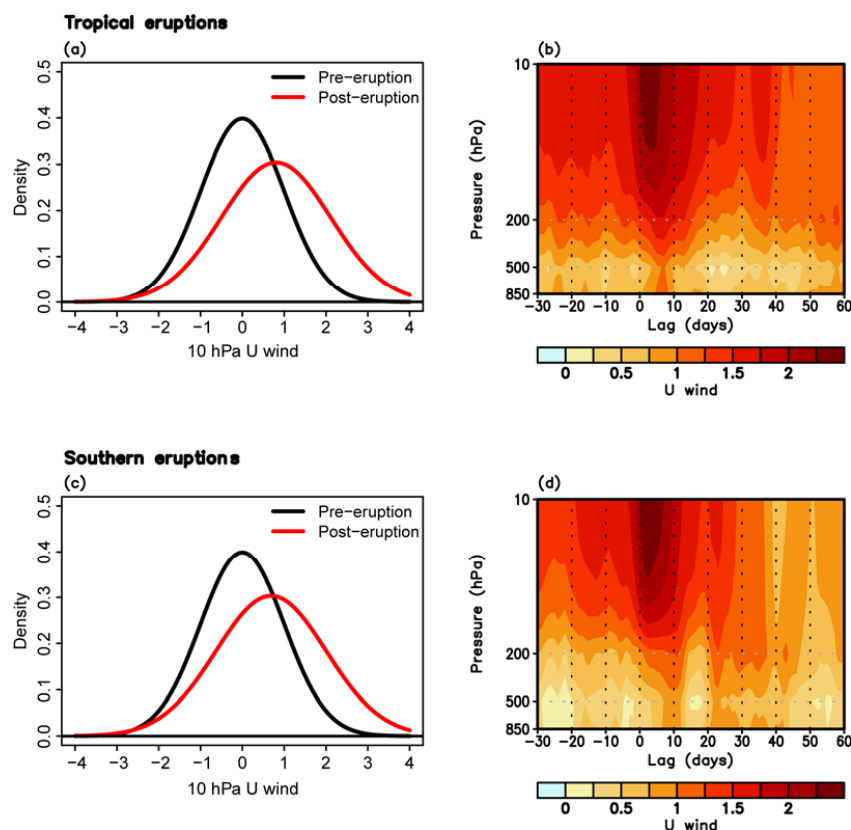
350 **Figure 8: Lower stratospheric to tropospheric zonal wind variation to (a, b) tropical; and (c, d) southern eruptions; (a, c) PDFs of daily 10 hPa zonal wind (60° N to 70° N averaged) anomalies during December to February in five year pre-eruption period (black) and first post-eruption year (red; December of Year 0 to February of Year +1); (b, d) vertical profile (850, 500, 200, and 10 hPa) of composited daily 10 hPa zonal wind (60° N to 70° N averaged) anomalies during -30 to +60 d (0 d represents initial date of strong polar vortex), following strong polar vortex events (n=48 and 36) for (b) tropical; and (d) southern eruptions, respectively.**

355

Figure 9 shows the relationship between the 10-hPa polar vortex and surface AO anomalies in D_0JF_{+1} after individual tropical or southern eruptions. Although both tropical and southern eruptions have a large spread, many samples are located in the first quadrant (i.e., strong polar vortex and positive AO). Importantly, this relationship between the 10-hPa polar vortex and surface AO anomalies in D_0JF_{+1} is statistically significant at the 1% significance level. This result suggests that tropical and southern

360 eruptions affect the NH surface climate by modulating the polar vortex and its downward coupling at D_0JF_{+1}. Figure 10 illustrates the surface climate responses of D_0JF_{+1} to volcanic eruptions. Similar to Fig. 7(a), westerly wind anomalies dominate the polar regions following tropical eruptions (Fig. 10(a)). These wind changes resemble those associated with a positive AO.

17

As a result of strong surface westerly anomalies from the northern North Atlantic to northern Eurasian continent, significant

warming occurs over northern Eurasia, with wetting in its northernmost parts (Figs. 10(b), (c)). Consistent with Fig. 7(d), much

365   weaker westerly wind anomalies appear over the polar regions after northern eruptions (Fig. 10(d)). These anomalies trigger

marginal changes to temperature and precipitation (Figs. 10(e), (f)). In contrast, after southern eruptions, westerly wind

anomalies expand more equatorward, with stronger AO-like sea-level pressure anomalies than the tropical eruption case (Fig.

10(g)), consistent with Fig. 7(g). These circulation anomalies induce extensive northern Eurasian winter warming and wetting

across a greater area than tropical eruptions as a result of more extended westerly wind anomalies (Figs. 10(h), (i)).
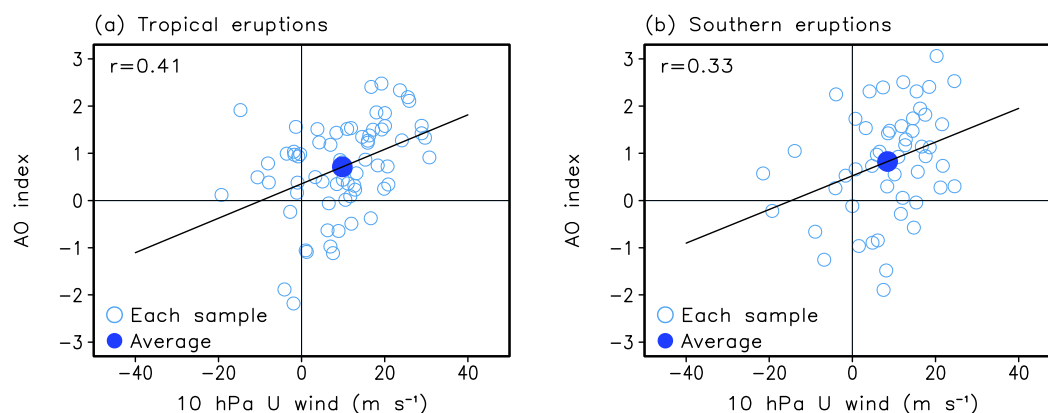
370

Figure 9: Scatterplots of 10 hPa zonal wind (60° N to 70° N averaged) and AO index anomalies at first boreal winter (December of Year 0 to February of Year +1) following (a) tropical (n=68); and (b) southern (n=51) eruptions. AO index is defined as associated timeseries of the principal component of the first empirical orthogonal function mode for boreal winter (December to next year February) sea level pressure over the north of 20° N during the 850–1849 period. Empty blue dots indicate each sample while solid darker blue dots indicate the sample average. Correlation coefficients obtained from samples are presented together.
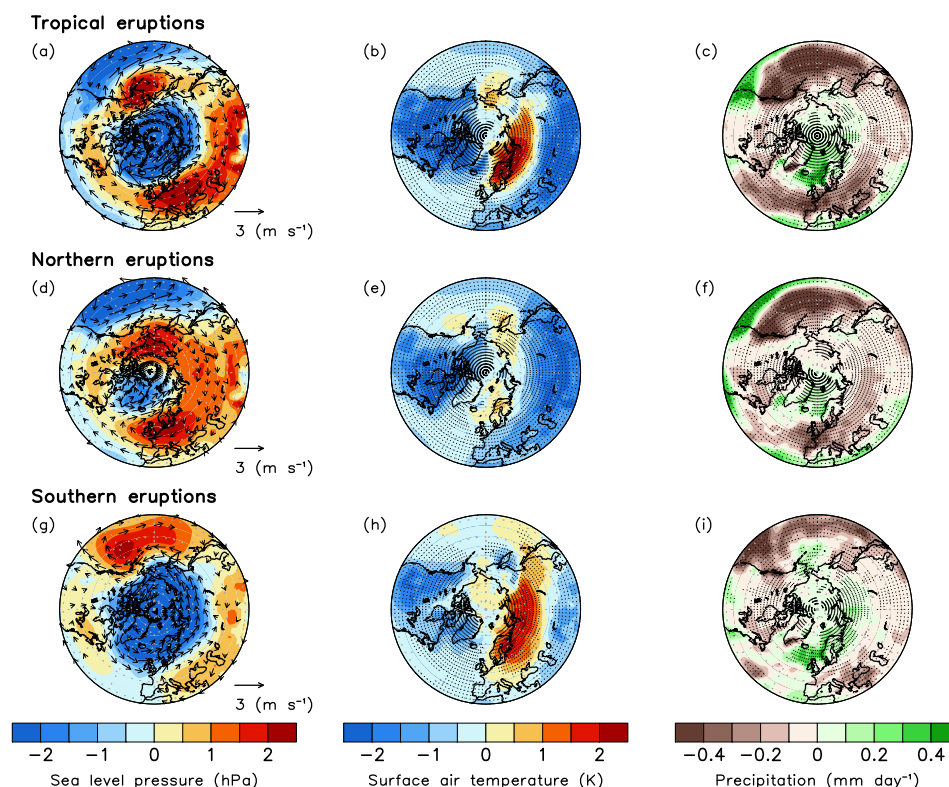
Figure 10: (a, d, g) Sea level pressure; (b, e, h) surface air temperature; and (c, f, i) precipitation anomalies over the NH mid-to-high latitude regions at first boreal winter (December of Year 0 to February of Year +1) following (a, d, g) tropical; (b, e, h) northern; and (c, f, i) southern eruptions. 850 hPa horizontal wind anomalies (vector) are shown together with sea level pressure fields, which are only shown when zonal or meridional wind shows a significant response beyond the 95 % confidence interval. For surface air temperature and precipitation, stippling indicates areas in which significant regional responses are beyond the 95 % confidence interval.

4. Summary and discussion

This study conducts a comprehensive analysis of climate responses to volcanic eruptions at different latitudes, based on the last millennium of volcanic eruptions available from CESM ensemble simulations. In particular, this study provides a first evaluation of how different eruption latitudes induce varying responses in ENSO and AO (through polar vortices), and thereby

exerting different degrees of influence on global monsoon precipitation and the northern Eurasian climate. Volcanic eruptions are classified as tropical, northern, and southern eruptions based on the NH and SH aerosol loading ratios. These three groups have different meridional structures of solar radiation perturbations and cause asymmetric climate response patterns between hemispheres.

395   The La Niña-like SST anomalies first appear during a few months after tropical eruptions. They are replaced by El Niño-like SST anomalies during the first boreal winter which peak during the subsequent boreal summer and winter. The MC drying is found to play a critical role in the El Niño response, inducing westerly winds over the equatorial western to central Pacific region. Northern eruptions tend to have westerly winds, while El Niño rapidly develops in the boreal summer due to the large southward shift of the ITCZ. Distinct seasonal variations also appear with double peaks of El Niño-like SST anomalies in YR0

400   and YR+1, and a short break in the spring of YR+1. Following southern eruptions, the delayed transition from the initial La Niña-like SST anomalies brings the gradual development of El Niño compared to tropical eruptions, with its mature development during the boreal summer and winter of YR+1. The El Niño SST anomalies induced by volcanic eruptions remotely contribute to global monsoon drying caused by volcanic eruptions. After tropical eruptions, El Niño intensifies NH and SH monsoon drying by approximately 52.5 % and 62.1 % at YR+1. Generally, El Niño contributions to NH and SH

405   monsoon drying are generally weaker than those of tropical eruptions from northern and southern eruptions respectively, because of the relatively weak El Niño responses to high-latitude eruptions. However, the hemispheric drying response is comparable to or stronger than that of tropical eruptions. The enhanced monsoon drying in the eruption hemisphere is found to be mainly due to a larger ITCZ displacement than in the tropical eruptions.

Tropical eruptions enhance polar vortices in both hemispheres due to lower stratospheric warming (increasing the meridional

410   temperature gradient), and its waveguide. Similar polar vortex changes are found during southern eruptions. Northern eruptions are observed to trigger no changes in the Arctic polar vortex because of the weaker equatorward wave propagation in the NH stratosphere. The calendar month in which northern eruptions occur crucially influences the variations in the Arctic polar vortex. The enhancement of the boreal–winter polar vortex increases the probability of positive AO in the troposphere after tropical and southern eruptions. This induces surface air temperature warming and increases precipitation over the northern

415   Eurasian continent. Following southern eruptions, the AO, Eurasian warming, and wetting responses are extended further southward due to more equatorward extended polar vortex variation.

Our results suggest that volcanic eruptions modulate summer monsoon and northern Eurasia winter climate by modulating ENSO and stratospheric polar vortex (accompanying AO) respectively. However, their influences largely depend on latitude of volcanic eruptions occurred. The results have important implications toward understanding the influence of structural

420   differences in stratospheric volcanic aerosols on the ENSO and AO, and their impacts on global and regional surface climate variability. A clearer understanding will improve decadal climate predictions following volcanic eruptions (Timmreck et al., 2016). The study also contains some limitations and caveats. This study does not consider the non-linearity of the climate response from volcanic forcing intensity. Future studies should consider both the latitude and intensity of volcanic eruptions. Large uncertainties remain in model simulations, particularly those related to the relatively strong ENSO simulated by the

Atmospheric
Chemistry
and Physics
Discussions

425 CESM-LME (Stevenson et al., 2016), treatment of volcanic aerosol forcing (Timmreck et al., 2010), and unknown volcanic eruption season (Gao et al., 2008). These uncertainties can produce substantially different climate responses (Predybaylo et al., 2020; Stevenson et al., 2017). The endorsed Model Intercomparison Project on climate response to volcanic forcing (VolMIP; Zanchettin et al., 2016) is expected to reduce such uncertainties, as the same volcanic forcings are applied to multiple models, which is the focus of a follow-up study.

430

Author contribution

S.-K.M. and S.P. conceived the research. S.P., S.-K.M. and S.-W.S. conducted the analysis and led the writing. S.-I.A., J.-S.K., and S.-W.Y. have contributed to the analysis and writing.

435 **Competing interests**

The authors declare that they have no conflict of interest.

References

445 Adams, J. B., Mann, M. E., and Ammann, C. M.: Proxy evidence for an El Niño-like response to volcanic forcing, Nature, 426, 274–278, https://doi.org/10.1038/nature02101, 2003.

Azoulay, A., Schmidt, H., and Timmreck, C.: The Arctic polar vortex response to volcanic forcing of different strengths, J. Geophys. Res.-Atmos., 126, e2020J034450, https://doi.org/10.1029/2020JD034450, 2021.

Baldwin, M. P., and Dunkerton, T. J.: Stratospheric harbingers of anomalous weather regimes, Science, 294, 581–584,

450 https://doi.org/10.1126/science.1063315, 2001.

21

Battisti, D. S., and Hirst, A. C.: Interannual variability in a tropical atmosphere–ocean model: Influence of the basic state, ocean geometry, and nonlinearity, J. Atmos. Sci., 46, 1687–1712, https://doi.org/10.1175/1520-0469(1989)046<1687:IVIATA>2.0.CO;2, 1989.

Bittner, M., Timmreck, C., Schmidt, H., Toohey, M., and Krüger, K.: The impact of wave-mean flow interaction on the
455   Northern Hemisphere polar vortex after tropical volcanic eruptions, J. Geophys. Res.-Atmos., 121, 5281–5297, https://doi.org/10.1002/2015JD024603, 2016.

Dai A., and Wigley, T. M. L.: Global patterns of ENSO-induced precipitation, Geophys. Res. Lett., 27, 1283–1286, https://doi.org/10.1029/1999GL011140, 2000.

Eddebbar, Y. A., Rodgers, K. B., Long, M. C., Subramanian, A. C., Xie, S.-P., and Keeling, R. F.: El Niño–like physical and
460   biogeochemical ocean response to tropical eruptions, J. Climate, 32, 2627–2649, https://doi.org/10.1175/JCLI-D-18-0458.1, 2019.

Emile-Geay, J., Seager, R., Cane, M. A., Cook, E. R., and Haug, G. H.: Volcanoes and ENSO over the past millennium, J. Climate, 21, 3134–3148, https://doi.org/10.1175/2007JCLI1884.1, 2008.

Fischer, E. M., Luterbacher, J., Zorita, E., Tett, S. F. B., Casty, C., and Wanner, H.: European climate response to tropical
465   volcanic eruptions over the last half millennium, Geophys. Res. Lett., 34, L05707, https://doi.org/10.1029/2006GL027992, 2007.

Gao, C., Robock, A., and Ammann, C.: Volcanic forcing of climate over the past 1500 years: An improved ice core-based index for climate models, J. Geophys. Res.-Atmos., 113, D23111, https://doi.org/10.1029/2008JD010239, 2008.

Holton, J. R., and Tan, H.-C.: The influence of the equatorial quasi-biennial oscillation on the global circulation at 50 mb, J.
470   Atmos. Sci., 37, 2200–2208, https://doi.org/10.1175/1520-0469(1980)037<2200:TIOTEQ>2.0.CO;2, 1980.

Hsu, P.-c., Li, T., and Wang, B.: Trends in global monsoon area and precipitation over the past 30 years, Geophys. Res. Lett., 38, L08701, https://doi.org/10.1029/2011GL046893, 2011.

Hsu, P.-c., Li, T., Murakami, H., and Kitoh, A.: Future change of the global monsoon revealed from 19 CMIP5 models, J. Geophys. Res.-Atmos., 118, 1247–1260, https://doi.org/10.1002/jgrd.50145, 2013.

475   Iles, C. E., and Hegerl, G. C.: The global precipitation response to volcanic eruptions in the CMIP5 models, Environ. Res.
        Lett., 9, 104012, https://doi.org/10.1088/1748-9326/9/10/104012, 2014.

        Joseph, R., and Zeng, N.: Seasonally modulated tropical drought induced by volcanic aerosol, J. Climate, 24, 2045–2060,
        https://doi.org/10.1175/2009JCLI3170.1, 2011.

        Khodri, M., Izumo, T., Vialard, J., Janicot, S., Cassou, C., Lengaigne, M., Mignot, J., Gastineau, G., Guilyardi, E., Lebas, N.,
480   Robock, A., and McPhaden, M. J.: Tropical explosive volcanic eruptions can trigger El Niño by cooling tropical
            Africa, Nat. Commun., 8, 778, https://doi.org/10.1038/s41467-017-00755-6, 2017.

        Lacis, A., Hansen, J., and Sato, M.: Climate forcing by stratospheric aerosols, Geophys. Res. Lett., 19, 1607–1610,
        https://doi.org/10.1029/92GL01620, 1992.

        Lim, H.-G., Yeh, S.-W., Kug, J.-S., Park, Y.-G., Park, J.-H., Park, R., and Song, C.-K.: Threshold of the volcanic forcing that
485   leads the El Niño-like warming in the last millennium: results from the ERIK simulation, Clim. Dynam., 46, 3725–
            3736, https://doi.org/10.1007/s00382-015-2799-3, 2016.

        Liu, F., Chai, J., Wang, B., Liu, J., Zhang, X., and Wang, Z.: Global monsoon precipitation responses to large volcanic
        eruptions, SCI. REP.-UK., 6, 24331, https://doi.org/10.1038/srep24331, 2016.

        Liu, F., Li, J., Wang, B., Liu, J., Li, T., Huang, G., and Wang, Z.: Divergent El Niño responses to volcanic eruptions at different
490   latitudes over the past millennium, Clim. Dynam., 50, 3799–3812, https://doi.org/10.1007/s00382-017-3846-z, 2018.

        Maher, N., McGregor, S., England, M. H., and Gupta, A. S.: Effects of volcanism on tropical variability, Geophys. Res. Lett.,
        42, 6024–6033, https://doi.org/10.1002/2015GL064751, 2015.

        McGregor, S. and Timmermann, A.: The effect of explosive tropical volcanism on ENSO. J. Climate, 24, 2178–2191,
        https://doi.org/10.1175/2010JCLI3990.1, 2011.

495   Ohba, M., Shiogama, H., Yokohata, T., and Watanabe, M.: Impact of strong tropical volcanic eruptions on ENSO simulated
        in a coupled GCM, J. Climate, 26, 5169–5182, https://doi.org/10.1175/JCLI-D-12-00471.1, 2013.

        Oman, L., Robock, A., Stenchikov, G., Schmidt, G. A., and Ruedy, R.: Climatic response to high-latitude volcanic eruptions,
        J. Geophys. Res.-Atmos., 110, D13103, https://doi.org/10.1029/2004JD005487, 2005.

Otto-Bliesner, B. L., Brady, E. C., Fasullo, J., Jahn, A., Landrum, L., Stevenson, S., Rosenbloom, N., Mai, A., and Strand, G.:
500   Climate variability and change since 850 CE: An ensemble approach with the Community Earth System Model, B.
          Am. Meteorol. Soc., 97, 735–754, https://doi.org/10.1175/BAMS-D-14-00233.1, 2016.

Paik, S., and Min, S.-K.: Climate responses to volcanic eruptions assessed from observations and CMIP5 multi-models, Clim.
          Dynam., 48, 1017–1030, https://doi.org/10.1007/s00382-016-3125-4, 2017.

Paik, S., and Min, S.-K.: Assessing the impact of volcanic eruptions on climate extremes using CMIP5 models, J. Climate, 31,
505   5333–5349, https://doi.org/10.1175/JCLI-D-17-0651.1, 2018.

Paik, S., Min, S.-K., Iles, C. E., Fischer, E. M., and Schurer, A. P.: Volcanic-induced global monsoon drying modulated by
          diverse El Niño responses, Science Advances, 6, eaba1212, https://doi.org/10.1126/sciadv.aba1212, 2020.

Pausata, F. S. R., Chafik, L., Caballero, R., and Battisti, D. S.: Impacts of high-latitude volcanic eruptions on ENSO and
          AMOC, P. Natl. Acad. Sci. USA, 112, 13784–13788, https://doi.org/10.1073/pnas.1509153112, 2015.

510 Predybaylo, E., Stenchikov, G., Wittenberg, A. T., and Osipov, S.: El Niño/Southern Oscillation response to low-latitude
          volcanic eruptions depends on ocean pre-conditions and eruption timing, Communications Earth & Environment, 1,
          12, https://doi.org/10.1038/s43247-020-0013-y, 2020.

Robock, A.: Volcanic eruptions and climate, Rev. Geophys., 38, 191–219, https://doi.org/10.1029/1998RG000054, 2000.

Robock, A., and Mao, J.: Winter warming from large volcanic eruptions, Geophys. Res. Lett., 19, 2405–2408,
515   https://doi.org/10.1029/92GL02627, 1992.

Robock, A., and Mao, J.: The volcanic signal in surface temperature observations, J. Climate, 8, 1086–1103,
          https://doi.org/10.1175/1520-0442(1995)008<1086:TVSIST>2.0.CO;2, 1995.

Stenchikov, G. L., Kirchner, I., Robock, A., Graf, H.-F., Antuña, J. C., Grainger, R. G., Lambert, A., and Thomason, L.:
          Radiative forcing from the 1991 Mount Pinatubo volcanic eruption, J. Geophys. Res.-Atmos, 103, 13837–13857,
520   https://doi.org/10.1029/98JD00693, 1998.

Stenchikov, G., Robock, A., Ramaswamy, V., Schwarzkopf, M. D., Hamilton, K., and Ramachandran, S.: Arctic Oscillation
          response to the 1991 Mount Pinatubo eruption: Effects of volcanic aerosols and ozone depletion, J. Geophys. Res.-
          Atmos., 107, 4803, https://doi.org/10.1029/2002JD002090, 2002.

24

Stevenson, S., Otto-Bliesner, B., Fasullo, J., and Brady, E.: "El Niño like" hydroclimate responses to last millennium volcanic

525   eruptions, J. Climate, 29, 2907–2921, https:doi.org/10.1175/JCLI-D-15-0239.1, 2016.

Stevenson, S., Fasullo, J. T., Otto-Bliesner, B. L., Tomas, R. A., and Gao, C.: Role of eruption season in reconciling model

        and   proxy   responses   to   tropical   volcanism,   P.   Natl.   Acad.   Sci.   USA,   114,   1822–1826,

        https://doi.org/10.1073/pnas.1612505114, 2017.

Taylor, K. E., Stouffer, R. J., and Meehl, G. A.: An overview of CMIP5 and experiment design, B. Am. Meteorol. Sco., 93,

530   485–498, https://doi.org/10.1175/BAMS-D-11-00094.1, 2012.

Thompson, D. W. J., Baldwin, M. P., and Wallace, J. M., 2002: Stratospheric connection to Northern Hemisphere wintertime

        weather: Implications   for   prediction,   J.   Climate,   15,   1421–1428,   https://doi.org/10.1175/1520-

        0442(2002)015<1421:SCTNHW>2.0.CO;2, 2002.

Timmreck, C., Graf, H.-F., Lorenz, S. J., Niemeier, U., Zanchettin, D., Matei, D., Jungclaus, J. H., and Crowley, T. J.: Aerosol

535   size   confines   climate   response   to   volcanic   super-eruptions,   Geophys.   Res.   Lett.,   37,   L24705,

        https://doi.org/10.1029/2010GL045464, 2010.

Timmreck, C., Pohlmann, H., Illing, S., and Kadow, C.: The impact of stratospheric volcanic aerosol on decadal-scale climate

        predictions, Geophys. Res. Lett., 43, 834–842, https://doi.org/10.1002/2015GL067431, 2016.

Toohey, M., Krüger, K., Bittner, M., Timmreck, C., and Schmidt, H.: The impact of volcanic aerosol on the Northern

540   Hemisphere stratospheric polar vortex: mechanisms and sensitivity to forcing structure, Atmos. Chem. Phys., 14,

        13036–13079, https://doi.org/10.5194/acp-14-13063-2014, 2014.

Trenberth, K. E., and Dai, A.: Effects of Mount Pinatubo volcanic eruption on the hydrological cycle as an analog of

        geoengineering, Geophys. Res. Lett, 34, L15702, https://doi.org/10.1029/2007GL030524, 2007.

Wang, T., Guo, D., Gao, Y., Wang, H., Zheng, F., Zhu, Y., Miao, J., and Hu, Y.: Modulation of ENSO evolution by strong

545   tropical volcanic eruptions, Clim. Dynam., 51, 2433–2453, https://doi.org/10.1007/s00382-017-4021-2, 2018.

Zanchettin, D., Khodri, M., Timmreck, C., Toohey, M., Schmidt, A., Gerber, E. P., Hegerl, G., Robock, A., Pausata, F. S. R.,

        Ball, W. T., Bauer, S. E., Bekki, S., Dhomse, S. S., LeGrande, A. N., Mann, G. W., Marshall, L., Mills, M., Marchand,

        M., Niemeier, U., Poulain, V., Rozanov, E., Rubino, A., Stenke, A., Tsigaridis, K., and Tummon, F.: The model

intercomparison project on the climatic response to volcanic forcing (VolMIP): experimental design and forcing input

550   data for CMIP6, Geosci., Model Dev., 9, 2701–2719, https://doi.org/10.5194/gmd-9-2701-2016, 2016.

Zuo, M., Man, W., Zhou, T., and Guo, Z.: Different impacts of northern, tropical, and southern volcanic eruptions on the

tropical Pacific SST in the last millennium, J. Climate, 31, 6729–6744, https://doi.org/10.1175/JCLI-D-17-0571.1,

2018.

Zuo, M., Zhuo, T., and Man, W.: Hydroclimate responses over global monsoon regions following volcanic eruptions at

555   different latitudes, J. Climate, 32, 4367–4386, https://doi.org/10.1175/JCLI-D-18-0707.1, 2019a.

Zuo, M., Zhuo, T., and Man, W.: Wetter global arid regions driven by volcanic eruptions, J. Geophys. Res.- Atmos., 124,

13648–13662, https://doi.org/10.1029/2019JD031171, 2019b.